Howard Hughes Medical Institute

Published as: *Nature*. 2018 March 15; 555(7696): 397–401.

Gating mechanisms of acid sensing ion channels

Nate Yoder[a], **Craig Yoshioka**[b], and **Eric Gouaux**[a,c,*]

[a]Vollum Institute, Oregon Health & Science University, Portland, Oregon 97239, USA

[b]Department of Biomedical Engineering, Oregon Health and Science University, 2730 SW Moody Ave, Portland, Oregon 97201, USA

[c]Howard Hughes Medical Institute, Oregon Health & Science University, Portland, Oregon 97239, USA

Abstract

Acid sensing ion channels (ASICs) are trimeric[1], proton-gated[2,3] and sodiumselective[4,5] members of the epithelial sodium channel/degenerin (ENaC/DEG) superfamily of ion channels[6,7] and are expressed throughout vertebrate central and peripheral nervous systems. ASIC gating occurs on a millisecond time scale[8] and can be largely described by a simple mechanism composed of three states: high pH resting, low pH open and low pH desensitized[9]. While previously solved x-ray structures of ASIC1a elucidated the conformations of the open[10] and desensitized[1,11] states, the structure of the high pH, resting state as well as detailed mechanisms for activation and desensitization have remained elusive. Here we present resting state structures of homotrimeric chicken ASIC1a at high pH determined by x-ray crystallography and single particle cryo-electron microscopy, informing a comprehensive molecular mechanism for proton-dependent gating in ASICs. In the resting state, the thumb domain has moved outward relative to its position in the open and desensitized states, expanding the ‘acidic pocket’. Activation thus involves ‘closure’ of the thumb into the acidic pocket, expansion of the lower palm domain and an iris-like opening of the channel gate. Furthermore, we demonstrate how the β11-β12 linkers demarcating upper and lower palm domains serve as a molecular ‘clutch’, undergoing a simple rearrangement to permit rapid desensitization.

To form well-ordered crystals an ASIC in a high pH resting state, we employed the Δ25 construct of chicken ASIC1a. This construct includes residues 25-463 of the full-length polypeptide and retains proton-dependent gating activity (Figure 1A-B). Crystals of the Δ25 construct belonging to the $P2_12_12_1$ space group were grown at high pH in the presence of

---

*Correspondence to Eric Gouaux: gouauxe@ohsu.edu.

Author Contributions: N.Y. and E.G designed the project. N.Y. performed biochemistry, crystallography, and electrophysiology experiments. N.Y. and C.Y. performed cryo-EM data collection. C.Y. performed the cryo-EM data analysis. N.Y wrote the manuscript and all authors edited the manuscript.

Data Availability: The data that support the findings of this study are available from the corresponding author upon reasonable request. The coordinates for the Δ25 x-ray structures have been deposited in the Protein Data Bank under the accession codes 5KWU and 5WKV. The coordinates and associated volume for the cASIC1a cryo-EM reconstruction have been deposited in the Protein Data Bank and Electron Microscopy Data Bank under the ascension codes 6AVE and 7009, respectively.

Author Information: The authors declare no competing financial interests.

inhibitory cations Ba^{2+} or Ca^{2+}[12] and diffract to 2.95 and 3.2 Å, respectively (Extended Data Table 1).

The Δ25-Ba^{2+} and Δ25-Ca^{2+} structures are nearly identical, adhering to the canonical chalice-like architecture of open[10] and desensitized[1,11] channels. Individual subunits resemble a clenched fist composed of TMD, palm, wrist, finger, knuckle, thumb, and β-ball domains[1] (Figure 1C). Relative to open[10] and desensitized[1,11] channels, the resting state structure shows that the thumb and finger domains adopt conformations farther from the molecular threefold axis, giving rise to an expanded extracellular domain (ECD) (Figures 1D-E) and exposing an additional ~ 595 $Å^2$ of solvent accessible surface area per subunit. The ion channel gate is closed and bears a striking resemblance to the TMD structure of the desensitized channel (Figure 1E), indicating that pore architecture is conserved across non-conducting functional states and suggesting that TMD conformation is not directly pH-dependent.

Though the Δ25 construct is gated by protons, truncation of the amino- and carboxy-termini reduces selectivity for Na^+ and decreases the Hill slope of proton-dependent ion channel activation (Extended Data Figure 4). Point mutations on TM2b, within the cytoplasmic region of the ion channel, also reduce sodium selectivity[13]. Given the altered function of the Δ25 construct and the importance of residues on or near the cytoplasmic domains of the ion channel, we determined the structure of the full-length chicken ASIC1a channel (cASIC1a) in a resting state at high pH and in the presence of Ca^{2+} to a nominal resolution of 3.7 Å by cryo-EM (Figure 2A-D, Extended Data Figure 1, Extended Data Figure 2, Extended Data Table 2).

Despite their functional discrepancies, Δ25 and cASIC1a structures are almost identical at the present resolutions (Figure 2E-G). Moreover, the superior quality of the EM density map in regions of the channel that suffer from weak x-ray based electron density provides valuable and unbiased structural information for domains central to gating and ion permeation in ASIC1a, including the acidic pocket and the TMD (Figure 2C-D). Nevertheless, key features from the x-ray structure are conserved, including an expanded acidic pocket and closed gate (Figure 2C-G). Furthermore, in both x-ray and cryo-EM structures, TM2 helices undergo a domain swap permitting the Gly-Ala-Ser motif[14-16] (GAS belt) to adopt an extended conformation immediately below the primary channel gate (Figure 1, Figure 2, Extended Data Figure 3). Taken together, the conformation of the resting channel observed in our x-ray structures was not substantially effected by truncation of the cytoplasmic termini, model bias or crystal packing.

ASIC1a channels populate a resting, closed state at physiological pH and activate within milliseconds in response to extracellular acidosis[17,18]. Consistent with its proposed role in proton-dependent gating[1,19], the acidic pocket, a solvent-exposed and electrostatically negative cavity formed at subunit interfaces, adopts an expanded conformation in both x-ray and cryo-EM resting state structures. We speculate that this conformation is stabilized by hydrophobic and polar contacts across finger, thumb and palm domains (Figure 3A-B, Extended Data Figure 5A-B). Upon extracellular acidification, the thumb helices α4 and α5 shift towards the channel core as α5 undergoes a 12° lateral pivot about its amino-terminus,

anchoring its carboxy-terminus against the palm domain of a neighboring subunit (Extended Data Figure 5C). Rearrangements of thumb helices upon activation reduce the distance between titratable residues within the acidic pocket, permitting the formation of proton-mediated carboxyl-carboxylate pairings that stabilize the interface between thumb, finger and palm domains.

The collapse of the acidic pocket upon exposure to protons is transduced to the channel pore by way of the palm domain, a network of β-strands that comprise the core of the channel, link movements of the ECD to the pore domain and frame extracellular fenestrations that provide access for cations to the extracellular vestibule and pore mouth (Extended Data Figure 6). Activation initiates rearrangements across the ECD that manifest as ~ 5° counterclockwise rotations of individual subunits around a lateral scaffold comprised of the β-ball and upper palm domains (Figure 3C). The rotation of all subunits in concert leads to a flexing of the lower palm towards the plasma membrane, displacing β1 and β12 by ~ 4 Å and inducing a translation of TM1 and TM2a away from the molecular threefold axis (Figure 3D, Supplementary Video 1), culminating in the expansion of the extracellular fenestrations (Extended Data Figure 6). The pore profile of the resting channel harbors a closed gate along the threefold axis composed of primary constrictions at Asp 433 and Gly 436 (Extended Data Figure 7A-B). Proton-dependent rearrangements originating at the ECD facilitate channel activation via an iris-like opening of TM helices (Extended Data Figure 7C-D), shifting the carboxyl groups of Asp 433 by 5.3 Å and rupturing the resting channel gate (Extended Data Figure 7E-F).

To elucidate the contributions of acidic pocket collapse to pH-dependent gating, we utilized site-directed double cysteine substitutions with the goal of introducing a disulfide bridge at residues Thr 84 and Asn 357 to anchor the thumb domain to the palm domain of a neighboring subunit, arresting the acidic pocket in an expanded conformation. In whole-cell patch clamp experiments, reducing conditions recovered proton-dependent gating behavior, increasing the magnitude of proton-dependent currents when compared to ambient conditions (Figure 3E-F).

The observation that ASIC1a activation is blocked by an inter-subunit disulfide bond at the acidic pocket supports a previously proposed functional role for subunit-subunit interactions in ASIC1a channels[20], underscores the critical nature of the acidic pocket to ASIC1a gating and supports a simple gating scheme wherein pH-dependent contraction of the acidic pocket drives channel activation.

ASIC1a channels undergo nearly complete desensitization over hundreds of milliseconds[17,18]. Situated at the border of the upper and lower palm domains, the β1-β2 and β11-β12 linkers are important determinants of gating kinetics in ASIC channels[21-25]. The overall conformation of the β1-β2 and β11-β12 linkers in the resting state mimics that of the open channel (Figure 4A-B). In contrast to the similarities between resting and open states at β11-β12 linkers, however, the side chains of Leu 414 and Asn 415 ‘swap’ positions in the desensitized channel, resulting in a 9 Å reorientation of Leu 414 towards the central vestibule and inducing a striking rearrangement of β11-β12 linkers (Figure 4C)[26]. We therefore propose that the conformation of β11-β12 linkers adopted in the resting state

provides a structural link between upper and lower channel domains, enabling pH-dependent collapse of the acidic pocket, which occurs ~ 40 Å away from the plasma membrane, to drive activation. Furthermore, we speculate that rearrangement of the β11-β12 linkers enables desensitization during prolonged exposure to low pH by serving as a molecular clutch, decoupling the collapsed acidic pocket from the lower channel and allowing TM1 and TM2a to relax by 6 Å and 5 Å, respectively (Supplementary Video 2, Figure 4D), permitting the re-formation of the non-conducting ion channel. Accordingly, desensitization produces a "conformationallychimeric channel" bearing striking resemblance to the resting channel below the β11-β12 linkers (Figure 1D), and to the open channel above. Upon return to physiological pH, expansion of the acidic pocket initiates the return of β11-β12 linkers to their original conformation, reforming a resting channel primed for subsequent activation.

To explore the contribution of the β11-β12 linker rearrangement to desensitization in ASIC1a channels, we utilized site-directed double cysteine substitution to anchor Leu 414 to an adjacent residue on β1-β2 via a putative engineered disulfide bridge. Exposure to protons elicited an inward current from L86C/L414C channels that displayed an initial slow desensitizing component and gave way to a sustained current despite continued exposure to protons (Figure 4E). Taken together, our data are consistent with Leu 414 and β11-β12 linkers separating from the neighboring β1-β2 linkers upon continued exposure to protons, and with this region playing a central role in the mechanism of desensitization.

Here we present x-ray and cryo-EM structures of ASIC1a channels in a resting state at high pH and in the presence of inhibitory cations Ba^{2+} or Ca^{2+}. The structure of a resting channel, the last remaining unsolved functional state of ASIC1a, unites our molecular understanding of the canonical functional states of ASIC1a channels and informs a comprehensive molecular model for pH-dependent gating mechanics (Figure 5). Moreover, in concert with the structure of the full-length cASIC1a in a resting state, our data suggest the TM2 domain swap and GAS belt as functional characteristics of ASIC1a architecture.

At physiological pH, ASIC1a channels largely populate a resting state with a pore closed to ion permeation and an expanded acidic pocket. Upon exposure to low pH, the acidic pocket adopts a collapsed conformation as α5 pivots towards the channel core to enable proton-mediated carboxyl-carboxylate pairings between thumb and finger domains. The collapse of the acidic pocket initiates coordinated movements throughout the ECD that manifest as lateral rotations of individual subunits around their upper palm domain scaffold. Rotation of all subunits in concert displaces the β1 and β12 strands of the lower palm domain towards the membrane and away from the molecular threefold axis. This shift of the lower palm domain results in an expansion of the extracellular fenestrations and an iris-like opening of the channel gate, expanding the GAS belt and allowing ions to pass through the channel pore.

ASIC1a channels undergo rapid and complete desensitization at low pH. Continued exposure to protons results in a swap in sidechain orientation for Leu 414 and Asn 415 residues, inducing a substantial rearrangement of the β11-β12 linkers demarcating upper and lower palm domains. Reorganization of palm domain linkers uncouples the low pH conformation of the upper ECD from the lower channel, allowing TM helices to relax back

into a resting-like conformation and forming a desensitized channel insensitive to protons. Re-priming ASIC1a channels for activation requires the removal of protons. We hypothesize that, upon return to physiological pH values, electrostatic repulsion stemming from the deprotonation of titratable acidic residues drives the expansion of the acidic pocket, permitting β11-β12 to revert back to a non-swapped conformation and recovering proton sensitivity upon formation of a resting channel.

Our results augment previous studies of gating mechanics in ASICs that suggest activation-induced movements at the acidic pocket as well as roles for the lower palm domain and β11-β12 linkers in desensitization[27-29]. By contrast, atomic force microscopy studies[30] indicate that human ASIC1a channels undergo a height increase of the ECD upon activation, a conformational change that has so far not been observed by analysis of x-ray crystallographic and cryo-EM structures of chicken ASIC1a. Nevertheless, the high cooperativity by which protons activate cASIC1a is consistent with multiple resting states characterized by varying degrees of protonation, suggesting that our current experimental structures represent an average over an ensemble of protein conformations. As ASICs are structurally the most well characterized members of the ENaC/DEG superfamily of ion channels, our studies provide fundamental insights into the mechanisms of gating and modulation of the entire superfamily.

Methods

Receptor construct, expression and purification

The Δ25 crystallization construct has 24 residues removed from the amino-terminus and 64 residues removed from the carboxy-terminus. Recombinant Δ25 protein was expressed in HEK293S GnTI$^-$ cells by way of baculovirus-mediated gene transduction. HEK293S GnTI$^-$ cells, in suspension culture, were grown to a density of 3.5×10^6 ml^{-1} and infected with P3 virus. After 8 hours of culture at 37°C, sodium butyrate was added to 10 mM final concentration and the temperature was shifted to 30°C. After 48 hours of expression, cells were collected by centrifugation, washed with phosphate buffered saline (PBS), and resuspended in Tris buffered saline containing protease inhibitors (TBS; 150 mM NaCl, 20 mM Tris pH 8.0, 1 mM phenylmethylsulfonyl fluoride, 0.05 mg ml^{-1} aprotinin, 2 μg ml^{-1} pepstatin A, and 2 μg ml^{-1} leupeptin). Cells were disrupted via sonication and membrane fractions were isolated by ultracentrifugation. cASIC1a channels were expressed in cell culture similar to the Δ25 construct yet without membrane fraction isolation.

Membrane pellets (Δ25) were resuspended in TBS buffer with protease inhibitors, homogenized, and solubilized in 40 mM *n*-dodecyl β-D-maltoside (DDM) for 1 hour at 4°C. cASIC1a channels were solubilized in an identical manner immediately after cell disruption via sonication. The solubilized material was clarified by ultracentrifugation and the supernatant was incubated in metal ion affinity resin for 1.5 hours at 4°C with 10 mM imidazole. Co^{2+} resin was packed into a column and subjected to three column volume wash steps with buffer containing 300 mM NaCl, 20 mM Tris pH 8.0, 1 mM DDM, and 10 mM imidazole followed by three additional column volume washes with buffer containing 300 mM NaCl, 20 mM Tris pH 8.0, 1 mM DDM, and 30 mM imidazole. Bound protein was eluted with 300 mM NaCl, 20 mM Tris pH 8.0, 1 mM DDM, and 250 mM imidazole.

Cleavage of the histidine-tagged enhanced green fluorescent protein (EGFP) tag was achieved by thrombin digestion. The Δ25 protein was further purified by size-exclusion chromatography (SEC) using a mobile phase containing 300 mM NaCl, 20 mM Tris pH 8.0, 2 mM *n*-decyl β-D-thiomaltopyranoside (C10ThioM), 1 mM dithiothreitol (DTT), 0.2 mM cholesteryl hemisuccinate (CHS) and 5 mM $CaCl_2$ or $BaCl_2$. Peak fractions were collected and concentrated to ~3 mg ml^{-1}.

Crystallization

Cholesterol stocks were maintained at 50 mg ml^{-1} in chloroform and stored at -20°C. Cholesterol aliquots were removed from stock and placed under argon until visibly dry. Dried cholesterol aliquots of 6 mg were resuspended by adding 20 μl of an aqueous solution of 400 mM C10ThioM, followed by gentle stirring for 1 hour at 4°C[31]. Subsequently, 110 μl of purified Δ25 protein at 3 mg ml^{-1} was added to the cholesterol/detergent mixture and incubated for 16 hours at 4°C with gentle stirring. The protein mixture was clarified by two ultracentrifugation steps and used immediately for crystallization experiments. For the Δ25-Ca^{2+} structure, the protein was incubated with cholesterol (6 mg) resuspended in 20 μl of an aqueous solution of 200 mM DDM.

Crystals were obtained at 4°C by way of the hanging drop vapor diffusion method. Reservoir solution contained 100 mM Tris pH 8.5-9.5, 150 mM NaCl, 5-20 mM $CaCl_2$ or $BaCl_2$, and 29-33% (v/v) PEG 400. Drops were composed of 1:1, 1.5:1, 1.75:1, and 2:1 protein to reservoir ratios, respectively. Crystals typically appeared within 2 weeks. Crystals were cryoprotected by increasing the PEG 400 concentration to 36% (v/v), in the protein-containing drop, before flash cooling in liquid nitrogen.

Structure Determination

X-ray diffraction data sets were collected at the Advanced Light Source (ALS) beamline 5.0.2 and at the Advanced Photon Source (APS) beamline 24ID-C and diffraction was measured to ~ 2.95 Å and ~ 3.2 Å for Δ25 with Ba^{2+}, and Ca^{2+}, respectively.

Diffraction data were indexed, integrated, and scaled using XDS and XSCALE[32] software. Diffraction data from Δ25-Ca^{2+} crystals was processed with the microdiffraction assembly method[33]. The Δ25-Ba^{2+} and Δ25-Ca^{2+} structures were solved by molecular replacement using the PHASER program[34]. For both structures, the extracellular domain coordinates of the ΔASIC1 structure (PDB 2QTS) were used as a search probe. All models were built via iterative rounds of manual model building in Coot[35] and refinement in Phenix[36] until satisfactory model statistics were achieved. Ramachandran statistics for both Δ25-Ba^{2+} and Δ25-Ca^{2+} structures were 98.31% favored and 1.69% allowed with none disallowed. ‘Omit’ maps were employed throughout the building and refinement process and to verify the presence of the GAS domain swap within the second transmembrane domain helix.

Sample preparation, data acquisition, image processing, and model building for cryo-EM

cASIC1a was purified as described for Δ25 with the mobile phase for SEC containing 150 mM NaCl, 20 mM Tris pH 8.0, 1 DDM, 1 mM DTT, 0.2 mM CHS and 5 mM $CaCl_2$. Peak fractions were concentrated to 3.2 mg ml-1 and 2.5 μl of cASIC1a sample was applied to a

glow-discharged (15 mA for 60 s on carbon side) Quantifoil holey carbon grid (gold, 1.2 μm/1.3 μm hole size/hole space, 300 mesh), blotted for 3 s at 100% humidity with a Vitrobot Mark IV (FEI) and plunge frozen in liquid ethane cooled by liquid nitrogen.

Data were collected on a Titan Krios cryo-electron microscope (FEI) operating at 300 kV. Images were recorded on a Gatan K2 summit direct electron detector, positioned after an energy filter (20 eV slit width), in super resolution mode with a binned pixel size of 1.04 Å. Images were collected using the automated image acquisition software SerialEM[37] and dose-fractionated to 100 frames at 0.1 s per frame with a total exposure time and dose of 10 s and 40-50 $e^-/Å^2$, respectively. Nominal defocus values ranged from -1 to -3 μm.

Images were motion corrected and summed with UCSF MotionCor2[37] and defocus values were estimated with Gctf[39]. ~ 256000 particles were picked using DoGPicker[40] and followed by reference-free 2D classification in Relion[41] to remove broken particles and aggregates. From 2D classification, ~ 160000 particles were subjected to 3D refinement and classification (C1 symmetry) in Relion to eliminate particles containing some degree of conformational heterogeneity. Inspection of the resulting 3D classes revealed four well-resolved classes containing a total of 33991 particles, which were subjected to further 3D refinement and classification in Relion (C3 symmetry). Finally, a single class containing 26117 particles was carried over for final refinement in cisTEM[42] with C3 symmetry imposed. Refinement in cisTEM was limited to a resolution of 4.5Å (>=0.9 of the FSC) to prevent overfitting. A mask was used in cisTEM that did not exclude the outlying mask areas, but did filter them to a resolution of 30Å to reduce the influence of the micelle on alignment. The final resolution was estimated to be 3.7 Å based on FSC gold standard analysis in Relion. Local resolution was calculated using blocres from the Bsoft[43] package with a box size of 20 and a 0.5 FSC cutoff.

The Δ25-Ba^{2+} crystal structure was docked into the EM density map for the cASIC1a channel in Chimera[44] and served as a template for manual model building of the cASIC1a channel in Coot. Deteriorating density prevented unambiguous modeling of 103 residues corresponding to the channel's cytosolic domains, limiting extension of the model to 1 and 5 residues on the amino- and carboxy-termini, respectively. The final model contains residues 41-464 of chicken ASIC1a and was subjected to real-space refinement in Phenix[45] and concluded with a CC of 0.867 for all atoms.

Patch clamp recordings

Whole-cell patch clamp recordings were carried out on CHO-K1 cells 1-2 days after transfection of plasmid DNA encoding cASIC1a and EGFP separated by an internal ribosome entry site. For characterization of Δ25 channels and all I-V experiments, whole-cell patch clamp recordings were carried out on Sf9 cells 36-48 hours after infection with Δ25-EGFP or cASIC1a-EGFP P1 BacMam virus[46]. For all electrophysiology experiments individual cells were only used once for recording, no repeated measurements were taken from the same cell. Pipettes were pulled and polished to 2-4 MΩ resistance and were filled with internal solution containing (in mM): 150 KCl, 2 $MgCl_2$, 5 EGTA, and 10 HEPES pH 7.35. Unless noted, external solution contained (in mM): 150 NaCl, 2 $MgCl_2$, 2 $CaCl_2$, 8

Tris, and 4 MES. Membrane voltage was clamped at -60 mV. The Axopatch 200B amplifier was used for data acquisition and pClamp 10 software was used for trace analysis.

Extended Data

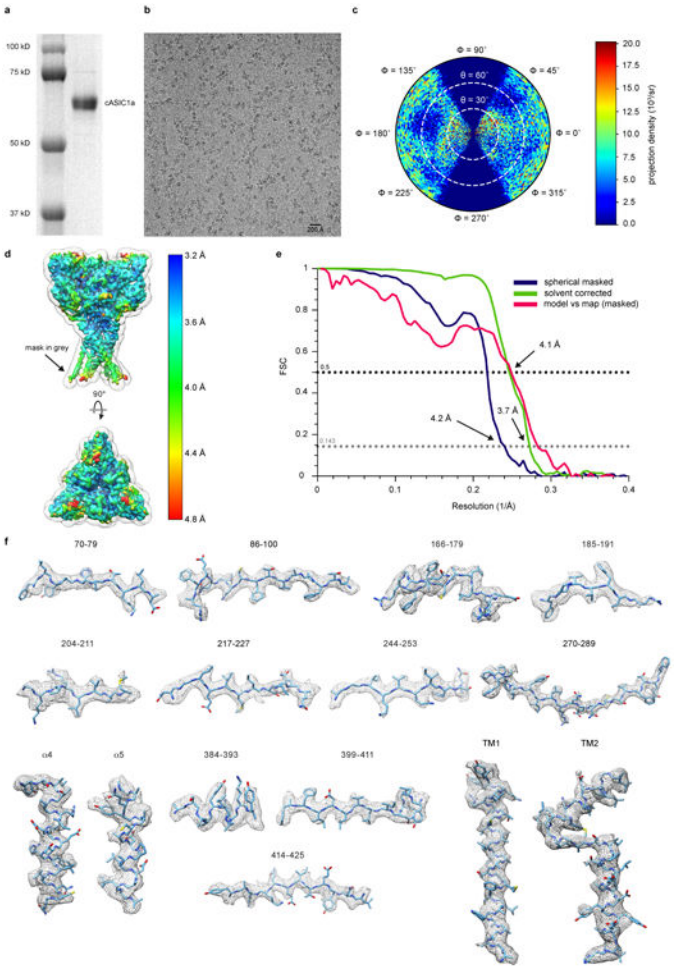

Extended Data Figure 1. Single particle cryo-EM of cASIC1a

a, SDS-PAGE gel of purified cASIC1a. **b,** Representative micrograph of cASIC1a channels embedded in vitreous ice. **c,** Angular distribution of particle projections, sphere size proportional to number of particles. **d,** Density map colored according to local resolution. **e,** Spherical masked and solvent corrected FSC curves for density maps and for the refined model to the final 3D reconstruction. **f,** Representative density for the cASIC1a reconstruction, identified by residue range or domain above.

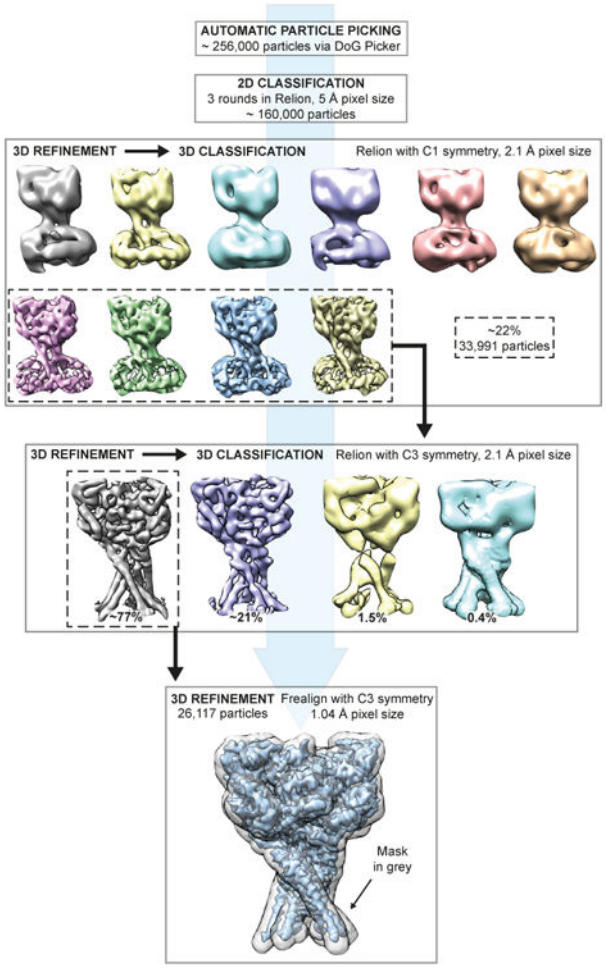

Extended Data Figure 2. Cryo-EM data processing workflow

Representative data processing steps for the cASIC1a reconstruction.

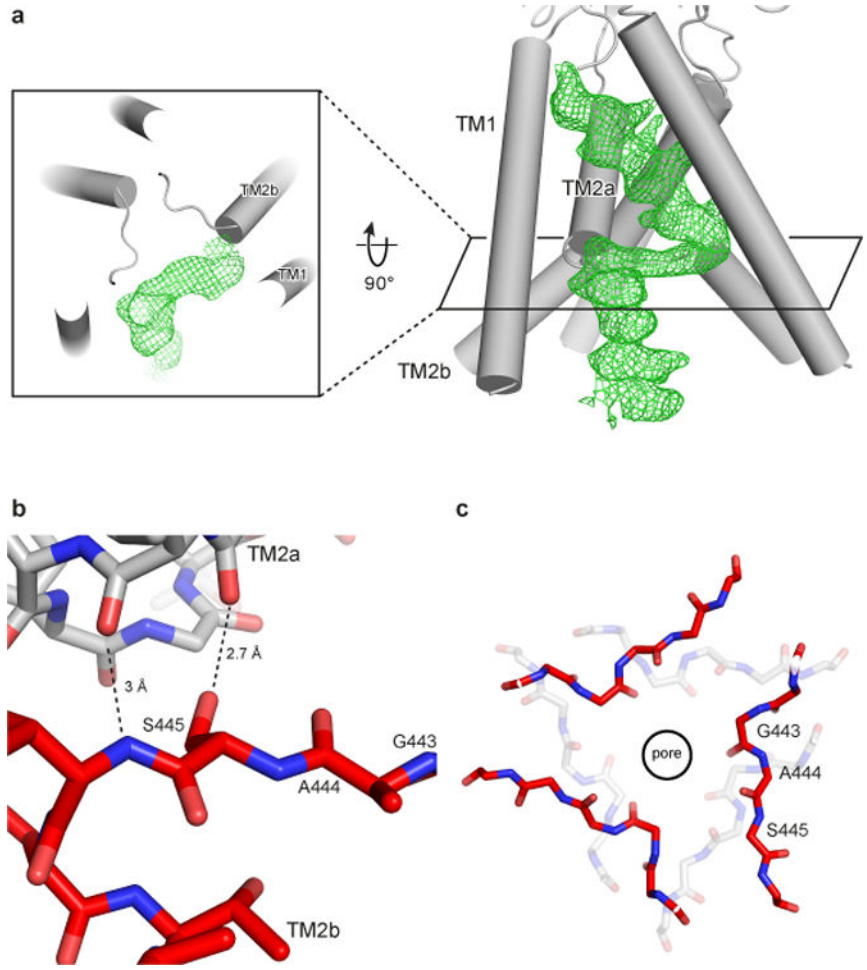

Extended Data Figure 3. GAS domain swap

a, Omit map Fo-Fc density contoured at 2σ for a domain-swapped TM2, top view shown in inset. **b,** Discontinuous TM2 helix stabilized by hydrogen bonds. **c,** Superposition of resting and open (pdb 4NTW, grey) channels demonstrates relative conformations of the GAS belt.

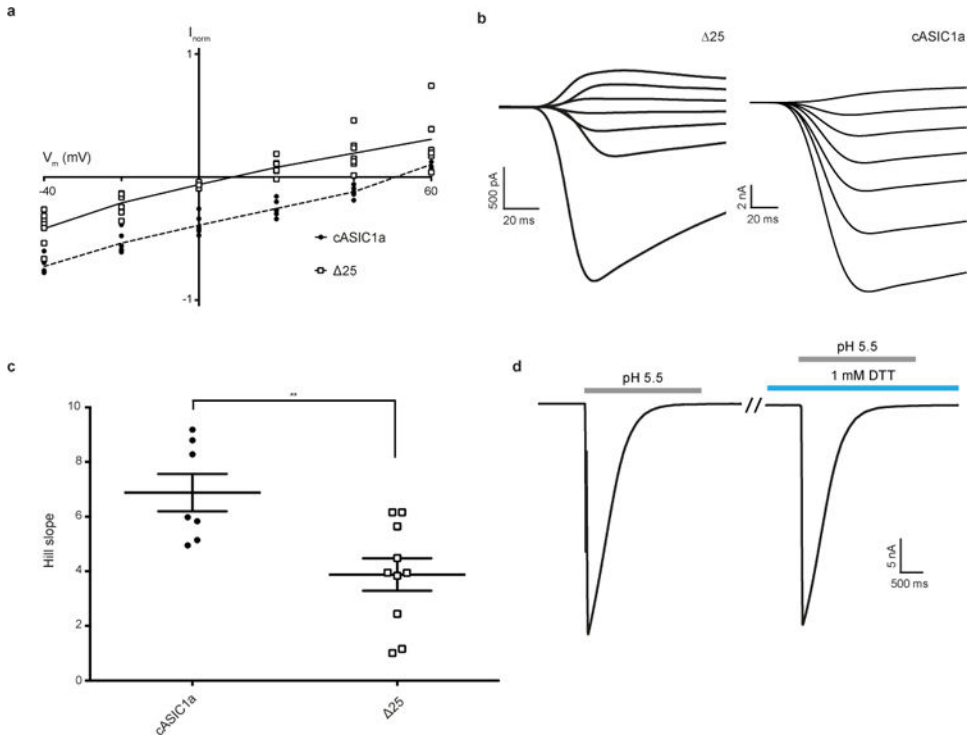

Extended Data Figure 4. Function of ASIC1a constructs

a, I-V relationship for cASIC1a and Δ25 constructs between -40 and 60 mV. Individual data points are displayed and were normalized to current amplitudes at -60 mV, lines represent mean, n = 7 cells for Δ25 and 6 cells for cASIC1a, experiments were replicated 7 times for Δ25 and 6 times for cASIC1a with similar results. **b,** Representative whole-cell patch clamp recordings at stepped potentials from -60 mV to +60 mV for Δ25 and cASIC1a, experiments were replicated 7 times for Δ25 and 6 times for cASIC1a with similar results. **c,** Unpaired t-test results (two-sided) comparing hill slopes of activation for Δ25 and cASIC1a channels. Error bars represent SEM and the center represents the mean, ** indicates $p \leq 0.01$, $p = 0.0054$ and 95% confidence interval = -4.949 to -1.053, n = 7 for cASIC1a and 10 for Δ25, experiments were replicated 7 times for cASIC1a and 10 times for Δ25 with similar results. **d,** Control experiment demonstrating cASIC1a currents evoked by step to low pH under reducing or ambient conditions, experiments were replicated 7 times with similar results. Data were collected from Sf9 cells infected with Δ25 or cASIC1a BacMam virus.

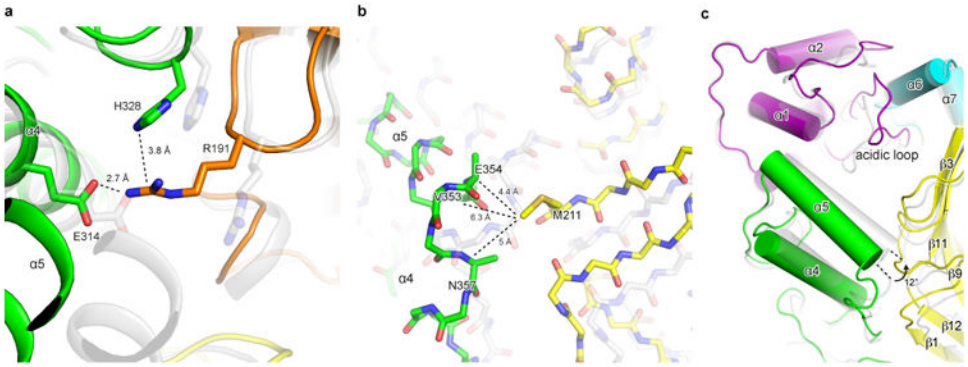

Extended Data Figure 5. Conformational changes at the acidic pocket

a-b, Superposition of resting and open (pdb 4NTW, grey) channels highlight interactions between Arg 191, Glu 314, and His 328 (**a**), as well as between Val 353, Glu 354 and Asn 357 with Met 211 on an adjacent subunit (**b**) that stabilize the expanded, high pH conformation of the acidic pocket. **c,** Local superposition (α1 and α2) of resting and open channels demonstrates α5 pivot upon activation.

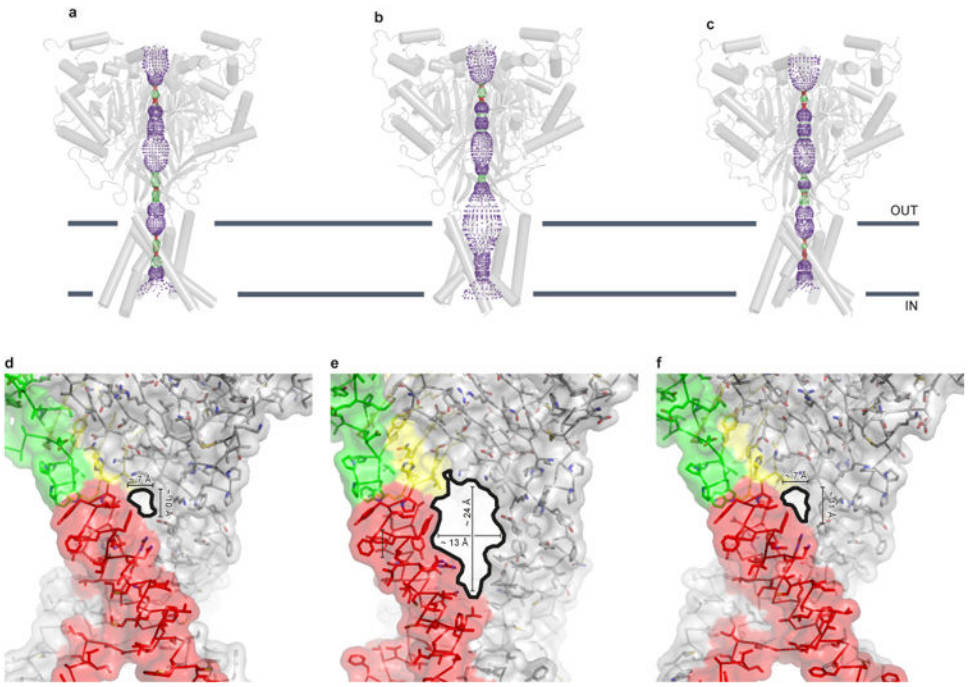

Extended Data Figure 6. State dependence of extracellular fenestrations

a-c, Resting (**a**), open (**b**) (pdb 4NTW), and desensitized (**c**) (pdb 4NYK) channel pore profiles calculated with HOLE software (pore radius: red < 1.15 Å < green < 2.3 Å < purple). **a-c,** Approximate fenestration sizes for resting (**d**), open (**e**), and desensitized (**f**) channels, Approximate fenestration edge outlined with a solid black line.

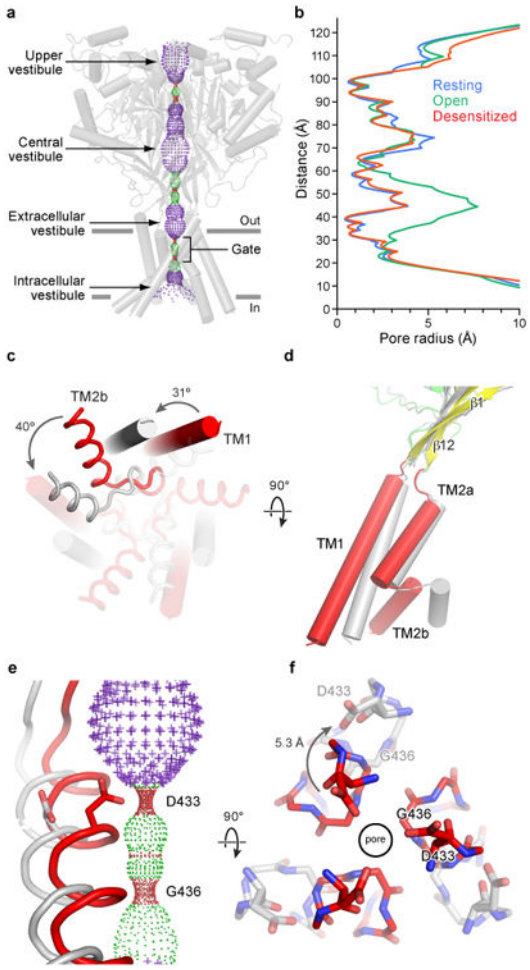

Extended Data Figure 7. State dependent pore conformation

a, Resting channel pore profile calculated with HOLE software (pore radius: red < 1.15 Å < green < 2.3 Å < purple). **b,** Plot of pore radius for resting, open (pdb 4NTW) and desensitized (pdb 4NYK) channels along the molecular threefold axis. **c-d,** Conformation of resting and open TMDs viewed from below (**c**) and the side (**d**). **e-f,** Resting and open gates viewed from the side (**e**) and above (**f**).

Extended Data Table 1

Crystallographic data collection and refinement statistics

	Δ25-Ba^{2+} Resting[†]	**Δ25-Ca^{2+}Resting**[‡]
Data collection		
Space group	$P2_12_12_1$	$P2_12_12_1$
Cell dimensions		
a, *b*, *c* (Å)	109.9, 130.4, 157.9	109.2 133.7 157.7
α, β, γ (°)	90.0, 90.0, 90.0	90.0, 90.0, 90.0
Resolution (Å)	50 - 2.95	100 - 3.20

	Δ25-Ba^{2+} Resting[†]	Δ25-Ca^{2+}Resting[‡]
R_{meas} (%)[*]	12.4 (549.8)	13.1 (58.1)
$I/\sigma I$[*]	15.39 (0.74)	7.05 (2.06)
Completeness (%)[*]	100 (100)	97.5 (99.1)
Redundancy	20.6	5.76
Refinement		
Resolution (Å)	25 - 2.95	25 - 3.2
No. reflections	48366	37646
R_{work} / R_{free}	0.226/0.258	0.287/0.297
No. atoms		
Protein	9247	9263
Ligand/ion	88	120
Water	0	0
B-factors		
Protein	145.62	157.29
Ligand/ion	194.47	187.53
Water	n/a	n/a
R.m.s. deviations		
Bond lengths (Å)	0.004	0.003
Bond angles (°)	0.701	0.688

[*] Highest resolution shell in parentheses.

[†] Two crystals were merged for the Δ25-Ba^{2+} resting state structure

[‡] Two crystals were merged for the Δ25-Ca^{2+} resting state structure and processed with microdiffraction assembly

5% of reflections were used for calculation of R_{free}.

Extended Data Table 2

Cryo-EM data collection, refinement and validation statistics

	cASIC1a (EMDB-7009) (PDB-6AVE)
Data collection and processing	
Magnification	135000
Voltage (kV)	300
Electron exposure (e–/Å^2)	40 - 50
Defocus range (μm)	-1 to -3
Pixel size (Å)	1.04
Symmetry imposed	C3
Initial particle images (no.)	~ 256000
Final particle images (no.)	26117
Map resolution (Å)	3.7
FSC threshold	0.143
Map resolution range (Å)	3.2 - 4.8
Refinement	
Initial model used (PDB code)	5WKU

	cASIC1a (EMDB-7009) (PDB-6AVE)
Model resolution (Å)	4.1
FSC threshold	0.5
Model resolution range (Å)	
Map sharpening *B* factor (Å^2)	-100
Model composition	
Non-hydrogen atoms	9657
Protein residues	423
Ligands	6
B factors (Å^2)	
Protein	100
Ligand	100
R.m.s. deviations	
Bond lengths (Å)	0.008
Bond angles (°)	0.946
Validation	
MolProbity score	1.75
Clashscore	6.0
Poor rotamers (%)	0.0
Ramachandran plot	
Favored (%)	95.02
Allowed (%)	4.98
Disallowed (%)	0.0

Supplementary Material

Refer to Web version on PubMed Central for supplementary material.

Acknowledgments

We thank A. Goehring, D. Claxton and I. Baconguis for initial construct screening and advice through all aspects of the project, L. Vaskalis for help with figures, H. Owen for manuscript preparation and all Gouaux lab members for their support. We acknowledge the Berkeley Center for Structural Biology and the Northeastern Collaborative Access Team for help with x-ray data collection. This research was supported by the National Institute of General Medical Sciences (5T32DK007680), and the National Institute of Neurological Disorders and Stroke (5F31NS096782 to N.Y. and 5R01NS038631 to E.G.). Additional support was provided by ARCS Foundation and Tartar Trust fellowships. E.G. is an Investigator with the Howard Hughes Medical Institute.

References

1. Jasti J, Furukawa H, Gonzales EB, Gouaux E. Structure of acid-sensing ion channel 1 at 1.9 Å resolution and low pH. Nature. 2007; 449:316–323. [PubMed: 17882215]
2. Krishtal OA, Pidoplichko VI. A receptor for protons in the nerve cell membrane. Neuroscience. 1980; 5:2325–2327. [PubMed: 6970348]
3. Waldmann R, Champigny G, Bassilana F, Heurteaux C, Lazdunski M. A proton-gated cation channel involved in acid-sensing. Nature. 1997; 386:173–177. [PubMed: 9062189]

4. Bassler EL, Ngo-Anh TJ, Geisler HS, Ruppersberg JP, Gründer S. Molecular and functional characterization of acid-sensing ion channel (ASIC) 1b. J Biol Chem. 2001; 276:33782–33787. [PubMed: 11448963]
5. Yermolaieva O, Leonard AS, Schnizler MK, Abboud FM, Welsh MJ. Extracellular acidosis increases neuronal cell calcium by activating acid-sensing ion channel 1a. Proc Natl Acad Sci U S A. 2004; 101:6752–6757. [PubMed: 15082829]
6. Kellenberger S, Schild L. Epithelial sodium channel/degenerin family of ion channels: a variety of functions for a shared structure. Physiol Rev. 2002; 82:735–767. [PubMed: 12087134]
7. Waldmann R, Lazdunski M. H(+)-gated cation channels: neuronal acid sensors in the NaC/DEG family of ion channels. Curr Opin Neurobiol. 1998; 8:418–424. [PubMed: 9687356]
8. Hesselager M, Timmermann DB, Ahring PK. pH Dependency and desensitization kinetics of heterologously expressed combinations of acid-sensing ion channel subunits. J Biol Chem. 2004; 279:11006–11015. [PubMed: 14701823]
9. Zhang P, Sigworth FJ, Canessa CM. Gating of acid-sensitive ion channel-1: release of Ca2+ block vs. allosteric mechanism. J Gen Physiol. 2006; 127:109–117. [PubMed: 16418400]
10. Baconguis I, Bohlen CJ, Goehring A, Julius D, Gouaux E. X-ray structure of acid-sensing ion channel 1-snake toxin complex reveals open state of a Na(+)-selective channel. Cell. 2014; 156:717–729. [PubMed: 24507937]
11. Gonzales EB, Kawate T, Gouaux E. Pore architecture and ion sites in acid-sensing ion channels and P2X receptors. Nature. 2009; 460:599–604. [PubMed: 19641589]
12. Babini E, Paukert M, Geisler HS, Gründer S. Alternative splicing and interaction with di- and polyvalent cations control the dynamic range of acid-sensing ion channel 1 (ASIC1). J Biol Chem. 2002; 277:41597–41603. [PubMed: 12198124]
13. Lynagh T, et al. A selectivity filter at the intracellular end of the acid-sensing ion channel pore. Elife. 2017; 6
14. Kellenberger S, Hoffmann-Pochon N, Gautschi I, Schneeberger E, Schild L. On the molecular basis of ion permeation in the epithelial Na+ channel. J Gen Physiol. 1999; 114:13–30. [PubMed: 10398689]
15. Kellenberger S, Gautschi I, Schild L. A single point mutation in the pore region of the epithelial Na + channel changes ion selectivity by modifying molecular sieving. Proc Natl Acad Sci U S A. 1999; 96:4170–4175. [PubMed: 10097182]
16. Snyder PM, Olson DR, Bucher DB. A pore segment in DEG/ENaC Na(+) channels. J Biol Chem. 1999; 274:28484–28490. [PubMed: 10497211]
17. Zhang P. Single channel properties of rat acid-sensitive ion channel-1alpha, -2a, and -3 expressed in Xenopus oocytes. The Journal of General Physiology. 2002; 120:553–566. [PubMed: 12356856]
18. Sutherland SP, Benson CJ, Adelman JP, McCleskey EW. Acid-sensing ion channel 3 matches the acid-gated current in cardiac ischemia-sensing neurons. Proc Natl Acad Sci U S A. 2001; 98:711–716. [PubMed: 11120882]
19. Sherwood T, et al. Identification of protein domains that control proton and calcium sensitivity of ASIC1a. J Biol Chem. 2009; 284:27899–27907. [PubMed: 19654327]
20. Gwiazda K, Bonifacio G, Vullo S, Kellenberger S. Extracellular subunit interactions control transitions between functional states of acid-sensing ion channel 1a. J Biol Chem. 2015; 290:17956–17966. [PubMed: 26070563]
21. Li T, Yang Y, Canessa CM. Leu85 in the beta1-beta2 linker of ASIC1 slows activation and decreases the apparent proton affinity by stabilizing a closed conformation. J Biol Chem. 2010; 285:22706–22712. [PubMed: 20479002]
22. Li T, Yang Y, Canessa CM. Asn415 in the beta11-beta12 linker decreases proton-dependent desensitization of ASIC1. J Biol Chem. 2010; 285:31285–31291. [PubMed: 20675379]
23. Li T, Yang Y, Canessa CM. Two residues in the extracellular domain convert a nonfunctional ASIC1 into a proton-activated channel. Am J Physiol Cell Physiol. 2010; 299:C66–73. [PubMed: 20427715]

24. Coric T, Zhang P, Todorovic N, Canessa CM. The extracellular domain determines the kinetics of desensitization in acid-sensitive ion channel 1. J Biol Chem. 2003; 278:45240–45247. [PubMed: 12947112]
25. Springauf A, Bresenitz P, Gründer S. The interaction between two extracellular linker regions controls sustained opening of acid-sensing ion channel 1. J Biol Chem. 2011; 286:24374–24384. [PubMed: 21576243]
26. Baconguis I, Gouaux E. Structural plasticity and dynamic selectivity of acid-sensing ion channel-spider toxin complexes. Nature. 2012; 489:400–405. [PubMed: 22842900]
27. Vullo S, et al. Conformational dynamics and role of the acidic pocket in ASIC pH-dependent gating. Proc Natl Acad Sci U S A. 2017; 114:3768–3773. [PubMed: 28320963]
28. Bonifacio G, Lelli CI, Kellenberger S. Protonation controls ASIC1a activity via coordinated movements in multiple domains. J Gen Physiol. 2014; 143:105–118. [PubMed: 24344244]
29. Ramaswamy SS, MacLean DM, Gorfe AA, Jayaraman V. Proton-mediated conformational changes in an acid-sensing ion channel. J Biol Chem. 2013; 288:35896–35903. [PubMed: 24196950]
30. Yokokawa M, Carnally SM, Henderson RM, Takeyasu K, Edwardson JM. Acid-sensing ion channel (ASIC) 1a undergoes a height transition in response to acidification. FEBS Lett. 2010; 584:3107–3110. [PubMed: 20621837]
31. Gourdon P, et al. HiLiDe—systematic approach to membrane protein crystallization in lipid and detergent. Crystal Growth & Design. 2011; 11:2098–2106.
32. Kabsch W. Xds. Acta Crystallogr D Biol Crystallogr. 2010; 66:125–132. [PubMed: 20124692]
33. Hanson MA, et al. Crystal structure of a lipid G protein-coupled receptor. Science. 2012; 335:851–855. [PubMed: 22344443]
34. McCoy AJ. Solving structures of protein complexes by molecular replacement with Phaser. Acta Crystallogr D Biol Crystallogr. 2007; 63:32–41. [PubMed: 17164524]
35. Emsley P, Lohkamp B, Scott WG, Cowtan K. Features and development of Coot. Acta Crystallogr D Biol Crystallogr. 2010; 66:486–501. [PubMed: 20383002]
36. Adams PD, et al. PHENIX: building new software for automated crystallographic structure determination. Acta Crystallogr D Biol Crystallogr. 2002; 58:1948–1954. [PubMed: 12393927]
37. Mastronarde DN. SerialEM: A program for automated tilt series acquisition on Tecnai microscopes using prediction of speciment position. Microscopy and Microanalysis. 2003; 9:1182–1183.
38. Zheng SQ, et al. MotionCor2: anisotropic correction of beam-induced motion for improved cryo-electron microscopy. Nat Methods. 2017; 14:331–332. [PubMed: 28250466]
39. Zhang K. Gctf: Real-time CTF determination and correction. J Struct Biol. 2016; 193:1–12. [PubMed: 26592709]
40. Voss NR, Yoshioka CK, Radermacher M, Potter CS, Carragher B. DoG Picker and TiltPicker: software tools to facilitate particle selection in single particle electron microscopy. J Struct Biol. 2009; 166:205–213. [PubMed: 19374019]
41. Scheres SH. RELION: Implementation of a Bayesian approach to cryo-EM structure determination. J Struct Biol. 2012; 180:519–530. [PubMed: 23000701]
42. Grigorieff N. Frealign: An exploratory tool for single-particle cryo-EM. Methods Enzymol. 2016; 579:191–226. [PubMed: 27572728]
43. Heymann JB. Bsoft: image and molecular processing in electron microscopy. J Struct Biol. 2001; 133:156–169. [PubMed: 11472087]
44. Goddard TD, Huang CC, Ferrin TE. Visualizing density maps with UCSF Chimera. J Struct Biol. 2007; 157:281–287. [PubMed: 16963278]
45. Afonine PV, Headd JJ, Terwilliger TC, Adams PD. New tool: phenix.real_space_refine. Computational Crysatllography Newsletter. 2013; 4:43–44.
46. Goehring A, et al. Screening and large-scale expression of membrane proteins in mammalian cells for structural studies. Nat Protoc. 2014; 9:2574–2585. [PubMed: 25299155]

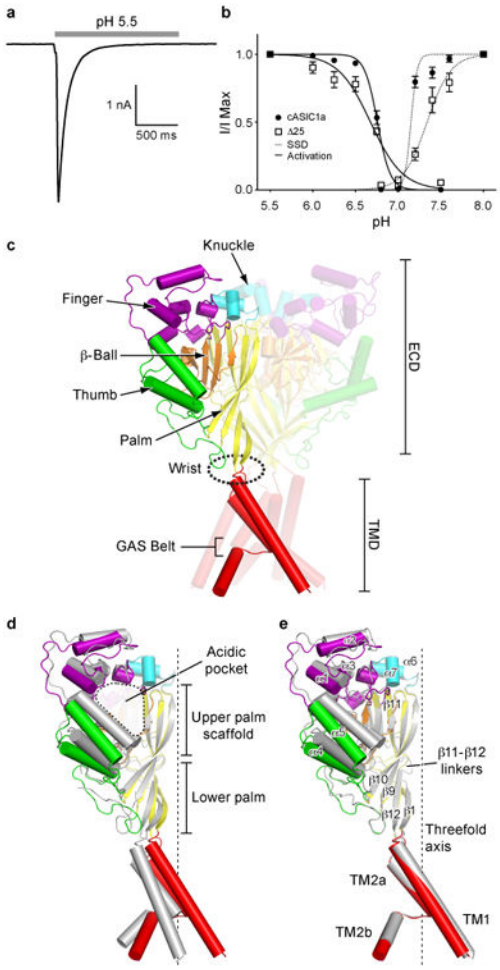

Figure 1. Architecture and function of a resting channel

a-b, Functional characterization of the Δ25 construct. Representative whole-cell patch clamp recording (**a**) from Δ25 channels activated by step to low pH and dose-response and steady state desensitization (SSD) curves (**b**) for Δ25 and cASIC1a channels. Data were collected from Sf9 cells infected with Δ25 or cASIC1a BacMam virus. Error bars represent SEM and the center represents the mean, n = 7 (activation) or 5 (SSD) cells for cASIC1a and 10 (activation) or 7 (SSD) cells for Δ25. Experiments were replicated 7 (activation) or 5 (SSD) times for cASIC1a and 10 (activation) or 7 (SSD) times for Δ25 with similar results. **c,** Structure of a Δ25 channel in a resting state at high pH, colored by domain. **d-e,** Single subunit superposition of resting channels with open (**d**) (pdb 4NTW, grey) and desensitized (**e**) (pdb 4NYK, grey) channels.

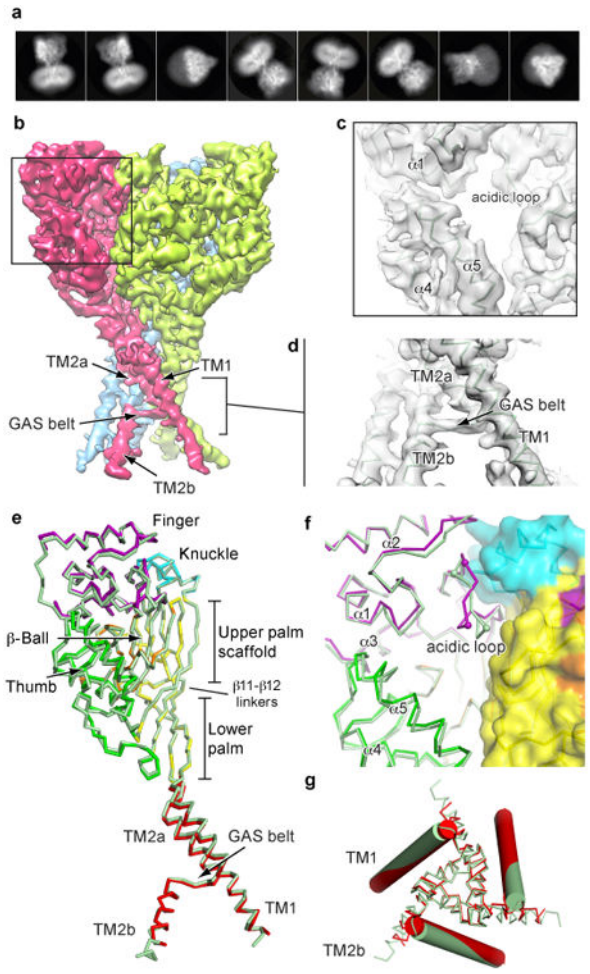

Figure 2. Cryo-EM structure of cASIC1a

a-d, Selected 2D classes (**a**) and cryo-EM density map (**b**) for cASIC1a with detail views of model and map for the acidic pocket (**c**) and TM2 domain swap **(d)**. **e,** single subunit superposition of Δ25 (grey) and cASIC1a channels. **f,** View of the acidic pocket from superposed Δ25 (grey) and cASIC1a channels, Gly 235 and Asp 238 α-carbon atoms are offset by ~ 3 Å and are shown as spheres. **g**, Top-down view of the TMD from superposed Δ25 (grey) and cASIC1a channels.

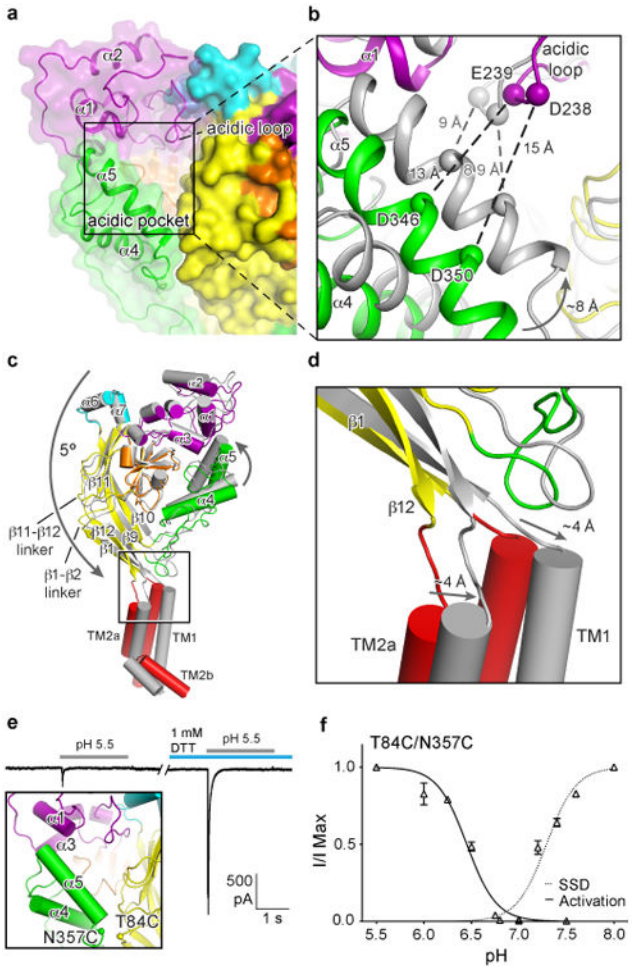

Figure 3. Acidic pocket collapse initiates channel activation

a-b, Resting channel acidic pocket (**a**) and superposition (**b**) with open channel (pdb 4NTW, grey). **c-d,** Single subunit superposition of resting and open channels demonstrates global (**c**) and lower palm domain (**d**) conformational changes associated with channel activation. **e,** Whole-cell patch clamp recording from T84C/N357C mutant channels, data were recorded from CHO-K1 cells transfected with cDNA for the T84C/N357C mutant channel or Sf9 cells infected with T84C/N357CBacMam virus, experiments were repeated 11 times with similar results. Schematic representation of site-directed cysteine substitutions shown in inset. **f,** Dose-response and SSD curves for T84C/N357C or cASIC1a channels. Data were collected from Sf9 cells infected with T84C/N357C or cASIC1a BacMam virus. For T84C/N357C channels, recordings were conducted in 1 mM DTT. Error bars represent SEM and the center represents the mean, n = 7 (activation) or 5 (SSD) cells for cASIC1a and 7 (activation) or 6 (SSD) cells for T84C/N357C. Experiments were replicated 7 (activation) or 5 (SSD) times for cASIC1a and 7 (activation) or 6 (SSD) times for Δ25 with similar results.

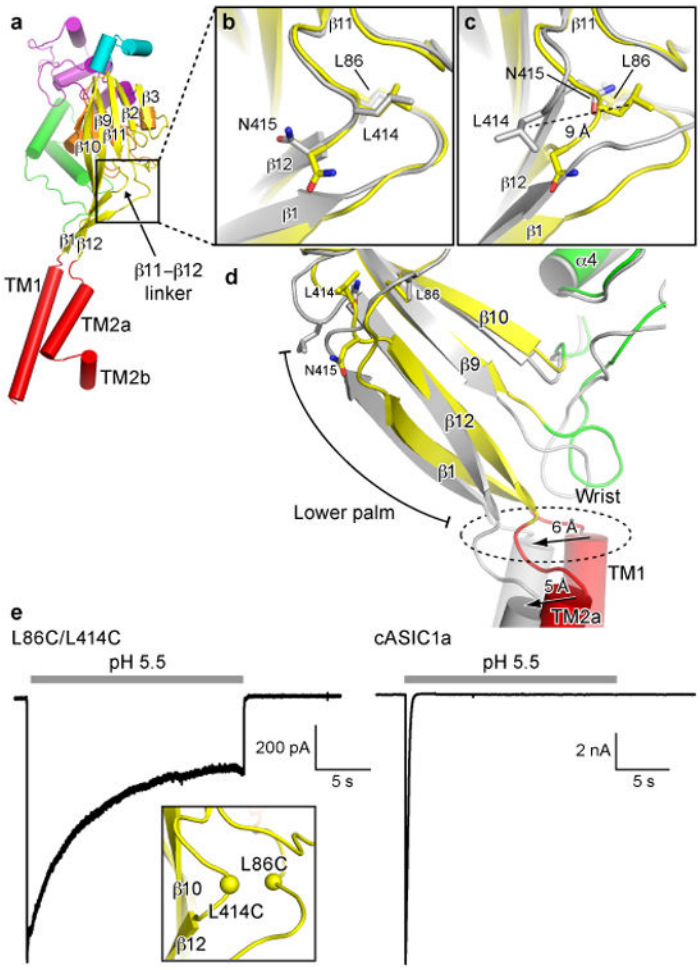

Figure 4. A molecular 'clutch' at β11-β12 linkers controls desensitization

a, Individual subunit of an open ASIC1a channel (pdb 4NTW). **b-c,** local alignments of an open channel with resting (**b**) and desensitized (**c**) (pdb 4NYK) channels (both in grey) demonstrate conformational rearrangements associated with desensitization. **d,** Comparison of lower palm and TMDs for open and desensitized (grey) channels. **e,** whole-cell patch clamp recordings from L86C/L414C and cASIC1a channels. Schematic representation of site-directed cysteine substitutions shown in inset. Data were collected from adherent CHO-K1 cells transfected with cDNA for mutant and cASIC1a channels, experiments were replicated 4 times with similar results.

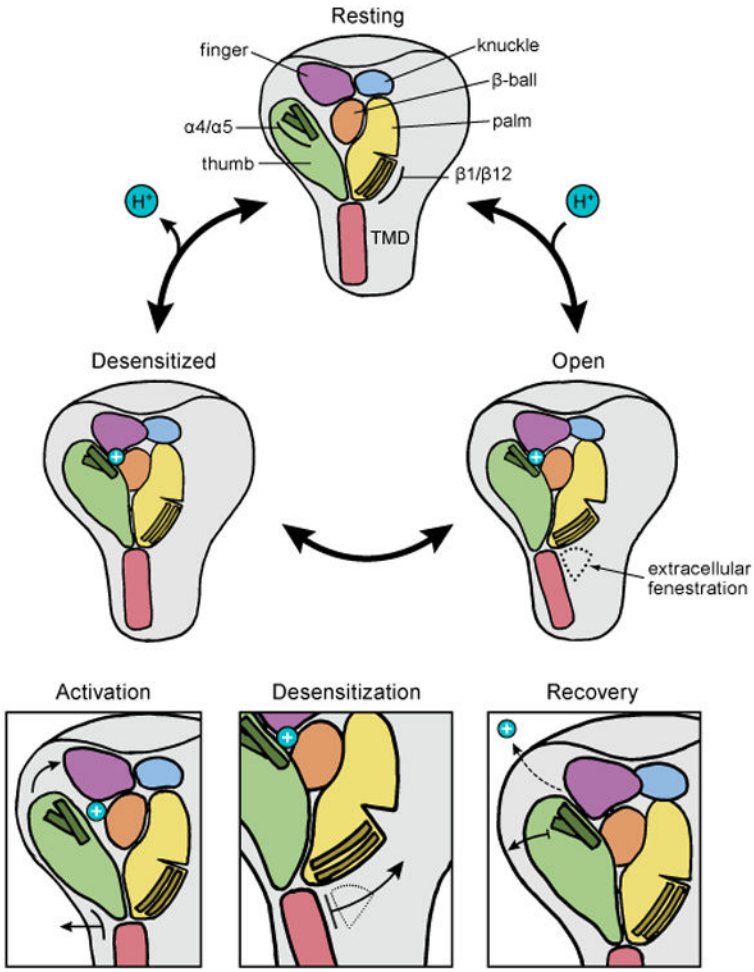

Figure 5. Gating scheme

Cartoon representation of proton-dependent gating cycle in ASIC1a channels.